Title

Sensitivity of a Continuum-Scale Porous Media Heat and Mass Transfer Model to the Spatial-Discretization Length-Scale of Applied Atmospheric Forcing Data

Journal

Water Resources Research, 55(4)

ISSN

0043-1397

Authors

Trautz, Andrew C
Illangasekare, Tissa H
Howington, Stacy
et al.

Publication Date

2019-04-01

DOI

10.1029/2018wr023923

Peer reviewed

Sensitivity of a Continuum-Scale Porous Media Heat and Mass Transfer Model to the Spatial-Discretization Length-Scale of Applied Atmospheric Forcing Data

Andrew C. Trautz[1,2], Tissa H. Illangasekare[1], Stacy Howington[2], and Abdullah Cihan[3]

[1] Center for Experimental Study of Subsurface Environmental Processes (CESEP), Department of Civil and Environmental Engineering, Colorado School of Mines, Golden, Colorado, USA, [2] U.S. Army Corps of Engineers Engineer Research and Development Center (ERDC), Vicksburg, Mississippi, USA, [3] Energy Geosciences Division, Lawrence Berkeley National Laboratory, Berkeley, California, USA

Correspondence to: A. C. Trautz, atrautz@mines.edu

Abstract

Fundamental process understanding and description of heat, mass, and momentum exchanges across the land-atmosphere interface in model boundary forcing parameterizations is critical to the simulation of near-surface soil moisture dynamics (e.g., bare-soil evaporation). This study explores the sensitivity of a continuum-scale porous media heat and mass transfer model to the spatial-discretization length-scales (i.e., spatial-resolution) of near-surface atmospheric data; the goal is to determine how much data are needed to force the model and adequately capture evaporative water losses and subsurface state variable distributions. The requisite atmospheric forcing data were taken from the high-resolution, precision bare-soil evaporation experiments of Trautz et al. (2018, https://doi.org/10.1029/2018WR023102). Simulation results demonstrated that shallow subsurface mass and heat transfer dynamics can be adequately captured with forcing data averaged over large length-scales, or a minimal number of measurements, provided that soil conditions are properly described. The soil moisture spatial distributions were found to be insensitive to horizontal variations in the forcing data. The model failed to capture small-scale trends observed experimentally; this did not impact the accuracy of total evaporative water loss estimates however. These results indicate that in future physical experimental efforts conducted at 1–10-m length-scales, there is no need to focus on the generation of high-spatial resolution atmospheric measurements—time and effort would be better spent in characterizing soil conditions and properties. Even though a theoretical foundation was not provided to directly extrapolate this work to the field scale, these findings have practical value in designing field data collection strategies.

1 Introduction

Soil moisture, or water stored in soils excluding groundwater, accounts for less than 0.05% of all freshwater on Earth by volume (Shiklomanov, 1993).

Despite representing such a small fraction of water, soil moisture, and the plethora of associated heat and mass transfer processes and feedback existing within the pedosphere, hydrosphere, biosphere, and atmosphere (e.g., bare-soil evaporation) are critical components of Earth's energy and water budgets across a wide range of spatiotemporal scales—hence its state variable designation (e.g., Berg et al., 2016; Betts, 2004; Brocca et al., 2012; Diremeyer et al., 2006; Picotte et al., 2007; Taylor & Ellis, 2006). The accurate simulation of shallow subsurface soil moisture dynamics, irrespective of the model scale or application, ultimately depends on the proper characterization and description of the exchanges coupling of heat, mass, and momentum across the land-atmosphere interface. When integrated over horizontal lengths, these exchanges are the net manifestation of a plethora of simultaneously occurring subgrid scale (i.e., relative to mesh size) transfer processes that vary spatially in response to local surface properties and atmospheric forcing conditions (Albertson & Parlange, 1999; Chen & Zhang, 2009; Diremeyer et al., 2006; Kato et al., 2007; Koster et al., 2009; Rodriguez-Iturbe et al., 2001).

A significant portion of research investigating impacts of atmospheric and strength of soil-atmosphere coupling on the subsurface or atmospheric state is conducted numerically (e.g., Davarzani et al., 2014; Entekhabi et al., 2010; Fetzer et al., 2016; Knist et al., 2016; Mosthaf et al., 2011; Santanello et al., 2009). This is due in part to the fact that the generation of high-resolution data sets needed to explore such coupling experimentally or validate model theory is difficult, if not at times impossible, to obtain in small laboratory column apparatuses or in the field setting which are constrained by issues related to scale, system control (e.g., soil property and climate variability), and cost (i.e., monetary, time) (Betts et al., 2015; Ferguson et al., 2012; Trautz, Illangasekare, Rodriguez-Iturbe, Heck, & Helmig, 2017; Western et al., 2004). Many of these issues are now being overcome with the development of specialized laboratory systems such as the Center for Experimental Study of Subsurface Processes wind tunnel-porous media test facility (e.g., Trautz, Illangasekare, & Rodriguez-Iturbe, 2017; Trautz et al., 2018; Trautz, Illangasekare, Rodriguez-Iturbe, Heck, & Helmig, 2017) and refinement of remote sensing (e.g., satellite, eddy-covariance) techniques (e.g., Ferguson et al., 2012; Hirschi et al., 2014; Hohenegger et al., 2009; Trigo et al., 2015). As more high-resolution data sets become readily available, new questions regarding model data assimilation will continue to emerge—for example, how much data are needed to test, refine, and drive numerical heat and mass transfer models across a wide range of spatiotemporal scales.

This study explores the sensitivity of a continuum-scale heat and mass transfer porous media model to the longitudinal spatial-discretization length-scales over which near-surface atmospheric forcing boundary condition data (i.e., air temperature, relative humidity, airflow) responsible for driving bare-soil evaporation are applied. This work was prompted by the recent findings

of Trautz et al. (2018) who observed longitudinal variations in the subsurface state in response to atmospheric feedback; one of the primary objectives of this work is to therefore determine the requisite spatial-resolution of atmospheric forcing measurements that actually need to be collected for different edaphic scenarios to adequately reproduce such evaporative water losses and soil moisture/temperature distributions with such a model. While it is not the intention, nor is there any theoretical foundation provided to directly extrapolate this work to the field scale, it is the belief of authors that the findings presented herein will have practical value in helping to inform future experimental data collection strategies and model data assimilation across multiple scales. The atmospheric data used to force the model (i.e., drive fluxes) in the present study were taken from a series of four high-resolution, large-scale (7.15 m) bare-soil evaporation data sets of Trautz et al. (2018) that were conducted in an experimental laboratory system consisting of a low-wind speed, climate-controlled micrometeorological wind tunnel interfaced with a soil tank. For each experimental scenario tested, a series of four simulations were run in which the atmospheric forcing data were averaged over different spatial-discretization length-scales and applied to the top boundary (i.e., soil surface) of the model. The model's sensitivity to the forcing data input spatial-resolution is assessed herein through a detailed intercomparison of simulation results and experimental measurements in the context of evaporative water loss, soil moisture distributions, and soil temperature distributions.

2 Numerical Experiments

In this section, the formulation of the numerical heat and mass transfer model is described, and the numerical experiments conducted for the present study presented. These two discourses are preceded however by a brief overview of bare-soil evaporation dynamics to provide the reader unfamiliar with this phenomenon needed insight for interpreting simulation results.

2.1 Bare-Soil Evaporation Overview

Bare-soil evaporation is a complex, multiscale, multiphase phenomenon involving both phase change (i.e., volatilization of liquid water) and water vapor transport (Philip & de Vries, 1957;van Brakel, 1980; Or et al., 2013). Phase change is driven by the chemical potential gradient existing between the liquid water phase and water vapor in the gas phase within a partially saturated pore space (Marek & Straub, 2001). At the macroscopic or REV scale, the process of evaporation is described as occurring in stages identifiable by the magnitude of the measured flux and dominant transport mechanisms (van van Brakel, 1980; Yiotis et al., 2006).

Stage I evaporation, or the constant-rate period, occurs in saturated or nearly saturated soils and is characterized by high, relatively constant fluxes driven primarily by local atmospheric demand (Hide, 1954). Stage I evaporation rates that decrease over time are usually characteristic of poorly

graded soils such as sands (Shahraeeni et al., 2012). The liquid water supporting the high evaporative fluxes is supplied via capillary flow to the soil surface from a retreating drying front within the soil body (Yiotis et al., 2004). Stage I evaporation will continue until the depth of this drying front surpasses the characteristic length of the soil, or the maximum depth over which liquid water is transported predominately by capillary action to the soil surface (Lehmann et al., 2008); beyond this point, the capillary force is exceeded by the combination of viscous and gravitational forces that act in the opposite direction (i.e., downward). As the soil continues to dry, it transitions to the falling rate period or Stage II evaporation in which the evaporative fluxes decline and become controlled primarily by the soil properties rather than the atmosphere (Shokri & Or, 2011). The evaporation rate decreases as a result of water transport becoming vapor diffusion-dominated and the rate of phase change being suppressed by the vapor lowering associated with increased capillary pressures (Ho, 2006; Yiotis et al., 2007).

2.2 Mathematical Model Formulation

A continuum-scale, multiphase, multicompositional, nonisothermal, nonequilibrium phase change, two-dimensional, porous media model was developed to simulate shallow subsurface heat and mass transfer dynamics. A mobile two-phase system composed of two compressible Newtonian fluids, liquid water (subscript *l*) and gas (subscript *g*) that exists in a rigid nondeformable porous medium (subscript *s*) is considered. The gas phase is treated as an idealized, homogenous binary mixture of air (composed of standard atmospheric constituents) and water vapor. Air is assumed to be immiscible in water (i.e., at equilibrium), so its compositional transport in the liquid water phase is not simulated.

2.2.1 Mass and Momentum Balance (Mass Transfer)

A mass balance for the liquid water and gas phases are expressed in terms of Darcy's law (Bear, 1972):

$$\frac{\partial(\rho_l S_l \phi)}{\partial t} + \nabla\cdot\left[-\rho_l \frac{\boldsymbol{K} k_{rl}}{\mu_l}(\nabla p_l + \rho_l \mathbf{g}\nabla z)\right] + q_{lv} = 0, \quad (1a)$$

$$\frac{\partial\left(\rho_g S_g \phi\right)}{\partial t} + \nabla\cdot\left[-\rho_g \frac{\boldsymbol{K} k_{rg}}{\mu_g}\left(\nabla p_g + \rho_g \mathbf{g}\nabla z\right)\right] - q_{lv} = 0, \quad (1b)$$

where ϕ (m^3/m^3) is the soil porosity, K (m^2) is the soil intrinsic permeability tensor, g (=9.82 m/s^2) is the gravity vector, z (m) is the height, and t (s) is the time. The variable q_{lv} ($kg\cdot m^{-3}\cdot s^{-1}$) is a source/sink term representing phase change (i.e., water volatilization, condensation); ρ_l is the temperature- and pressure-dependent density of liquid water (Kell, 1975); ρ_g (kg/m^3) is the temperature-, pressure-, and vapor concentration-dependent density of moist air (Davis, 1992); μ_l and μ_g (Pa/s) are the dynamic viscosities of the two phases (Poling et al., 2001); k_{rl} and k_{rg} (dimensionless) are the phase relative

permeabilities; and S_l and S_g (dimensionless) are the phase saturations. The liquid water and gas phase pressures which are related to each other through p_c (Pa), the soil capillary pressure ($p_c = p_g - p_l$). Note that as phase velocities in unsaturated soils are often slow (i.e., Re $\ll$ 1), dispersion was neglected in equations 1a and 1b (Shokri et al., 2008).

The liquid water saturation is related to capillary pressure via the water retention curve and can be mathematically described using one of many existing models. Given the importance of the hygroscopic soil moisture state in the shallow subsurface and the failure of classical water-retention models to capture conditions at low saturations, the Fayer and Simmons (1995) extension of the van Genuchten (1980) model is applied herein:

$$S_e(p_c) = \frac{S_l - S_{lr}}{1 - S_{lr}} = \begin{cases} \chi S_* + (1-\chi S_*)\left[1 + \left(\alpha\left|\frac{p_c}{\rho_l g}\right|\right)^n\right]^{-1+1/n} & \frac{p_c}{\rho_l g} > 0 \\ 1 & \frac{p_c}{\rho_l g} \leq 0 \end{cases}, \quad (2)$$

where S_e (dimensionless) is the effective saturation, S_{lr} (dimensionless) is the residual liquid phase saturation, S_* is the liquid phase saturation measured at p_c = 1 Pa, χ (dimensionless) accounts for the adsorption of the liquid phase to the soil grains, and α (m^{-1}) and n (dimensionless) are the van Genuchten parameters—the value of these latter two variables are determined from experimental column studies (Sakaki & Illangasekare, 2007). The gas phase saturation is by definition, expressed as $S_g = 1 - S_l$. The relative permeability of the liquid and gas phases present in equations 1a and 1b are expressed as a function of the effective soil saturation (equation 2) using the van Genuchten-Mualem model (Mualem, 1976; van Genuchten, 1980).

Water vapor is an essential component of the gas phase in the unsaturated zone of the porous media model. Assuming that water vapor transport occurs via both convection with the bulk gas phase and diffusion along vapor gradients, the mass balance for the vapor component of the gas phase can be written as

$$\phi\frac{\partial\left(\rho_g w_v S_g\right)}{\partial t} + \nabla\cdot\left[-\rho_g w_v \frac{\mathbf{K}k_{rg}}{\mu_g}\left(\nabla p_g + \rho_g \mathbf{g}\nabla z\right)\right] + \nabla\cdot\left(-D_v^*\rho_g \nabla w_v\right) - q_{lv} = 0, \quad (3)$$

where w_v (dimensionless) is a model primary unknown identified as the mass fraction of water vapor in the gas phase (i.e., ρ_v/ρ_g) in which ρ_v (kg/m^3) is the vapor density. The variable D_v^* (m^2/s) is the effective vapor diffusion coefficient defined as the product of the diffusion coefficient of water vapor in air ($D_v \approx 2.5 \times 10^{-5}$ m^2/s) and soil tortuosity (Millington & Quirk, 1961).

In traditional heat and mass transfer evaporative modeling, phase change (i.e., water volatilization and condensation) is often assumed to occur instantaneously, or that the system is always at equilibrium with respect to the vapor density (e.g., Campbell, 1985; Philip & de Vries, 1957; Whitaker,

1977). Experimental evidence (e.g., Bénet & Jouanna, 1982; Chammari et al., 2003; Ruiz & Bénet, 2001) has shown that this assumption may not be valid when soils are in a hygroscopic moisture state; a finite time is required to volatilize water as the phase change is limited by the high binding energy of the water absorbed to soil grains (Lozano et al., 2008; Ouedraogo et al., 2013). Nonequilibrium phase change, q_{lv}, can be described using one of several existing formulations. In this work, q_{lv} is defined according to a temperature- and soil water saturation-dependent formulation derived from the kinetic theory of gases (Zhang & Datta, 2004):

$$q_{lv} = \frac{\phi b(S_l - S_{lr})RT}{M_l}\left(\rho_v - \rho_{veq}\right), \quad (4)$$

where b (s/m^2) is a constant of proportionality, R (Pa·m^3·K^{-1}·mol^{-1}) is the universal gas constant, T (K) is the temperature, and M_l (kg/mol) is the molecular weight of water. For more information regarding nonequilibrium phase change, including the use of equation 4, the reader is referred to Trautz et al. (2015). The term ρ_{veq} (kg/m^3) represents the equilibrium vapor density expressed per Kelvin's equation:

$$\ln\left(\frac{\rho_{veq}}{\rho_{vs}}\right) = -\frac{p_c M_l}{\rho_l RT}, \quad (5)$$

where ρ_{vs} (kg/m^3) is the saturated vapor density estimated by the Antoine equation (Speight, 2005).

2.2.2 Energy Balance (Heat Transfer)

In general, heat transfer occurs within the soil by convective, conductive, and latent heat (due to phase change) mechanisms. Assuming local thermal equilibrium between phases (i.e., $T_l = T_g = T_s = T$), the energy balance of the system is written as (Whitaker, 1977)

$$\frac{\partial\left[\left(\rho c_p\right)^* T\right]}{\partial t} + \nabla\cdot\left[-\left(\rho c_p\right)_l \frac{\boldsymbol{K}k_{rl}}{\mu_l}(\nabla p_l + \rho_l \mathbf{g}\nabla z)T - \left(\rho c_p\right)_g \frac{\boldsymbol{K}k_{rg}}{\mu_g}\left(\nabla p_g + \rho_g \mathbf{g}\nabla z\right)T - \lambda^*\nabla T\right] + Lq_{lv} + Q_s = 0 \quad (6)$$

and solved for the temperature, another model primary unknown. The terms $(\rho c_p)_s$, $(\rho c_p)_l$, and $(\rho c_p)_g$ (J·kg^{-1}·K^{-1}) denote the phase heat capacities, L (≈2.45 × 10^6 J/kg) is the latent heat of vaporization of water, and Q_s (W/m^3) is the system heat loss/gains defined in terms of Newton's law of cooling. Given existing knowledge of the thermal properties and the experimental exterior tank temperatures, the associated heat loss coefficient was estimated using the average dimensionless Nusselt number. The term $(\rho c_p)^*$ corresponds to the effective heat capacity of the system defined here as summation of the individual phase heat capacities:

$$\left(\rho c_p\right)^* = (1-\phi)\left(\rho c_p\right)_s + \phi S_l\left(\rho c_p\right)_l + \phi(1-S_l)\left(\rho c_p\right)_g. \quad (7)$$

The effective thermal conductivity, λ^* ($W \cdot m^{-1} \cdot K^{-1}$), is calculated using the Campbell et al. (1994) model that accounts for both phase saturation and temperature in a weighted summation:

$$\lambda^* = \frac{(1-\phi)\omega_s\lambda_s + \phi S_l \omega_l \lambda_l + \phi(1-S_l)\omega_g \lambda_g}{(1-\phi)\omega_s + \phi S_l \omega_l + (1-S_l)\phi\omega_g}, \quad (8)$$

where λ_s, λ_l, and λ_g ($W \cdot m^{-1} \cdot K^{-1}$) are the phase thermal conductivities and ω_s, ω_l, and ω_g (dimensionless) are the weighting factors calculated according to Campbell et al. (1994).

2.2.3 Initial and Boundary Conditions

The soil tank used in Trautz et al. (2018) is represented by a two-dimensional model domain with identical depth and length. Following those physical experiments, at the start of each simulation, the water pressure is described as being hydrostatically distributed (i.e., $p_l = \rho_l g z$) and the soil fully saturated ($S_l = 1$). A total gas pressure equal to that of the atmospheric barometric pressure of Golden, Colorado (elevation 1,730 m) is assigned for the gas phase. An initial vapor concentration of zero is assigned to the entire model domain as the soil was fully saturated (i.e., $S_g = 0$). The initial soil temperature was set to the value measured at the start of each experimental scenario. Neumann boundary conditions, specifically zero heat and mass fluxes, are specified on the sides and bottom of the model domain for all phases and components. A zero-mass flux (i.e., no flow) condition is also assigned to the top of the model domain for the liquid water phase. The gas pressure is set equal to the atmospheric pressure at this location as well.

The water vapor flux, or evaporative flux E ($kg \cdot m^{-2} \cdot s^{-1}$), is specified by a resistance-based approach expressed in a formulation analogous to Ohm's law:

$$J_v = E = -\frac{\rho_v - \rho_{vs} RH(t)}{r_{bl}}, \quad (9)$$

where $RH(t)$ (dimensionless) is the time-dependent experimentally measured relative humidity and r_{bl} (s/m) is the boundary layer resistance. Note that a soil resistance term is not applied in this model so that the effects of the atmospheric resistance could be better explored. Given the design and scale of the experiments of Trautz et al. (2018) and goals of the present study, r_{bl} is specifically not defined in terms of aerodynamic resistance formulations traditionally applied in field-scale studies (e.g., Bittelli et al., 2008; Thom, 1972; van de Griend & Owe, 1994; Villagarcía et al., 2007; Zeng et al., 2011) but instead in terms of a scale-appropriate vapor diffusion-based formulation modeled after Schlünder (1988) and Haghighi and Or (2013):

$$r_{bl} = \frac{\delta + Pf(\theta_{surf})}{D_v}, \quad (10)$$

where D_v is the diffusion coefficient of water vapor in air and P (m) is the average soil pore size ($P = 0.5d\sqrt{\pi}$), where d (m) is the grain diameter

(Hamamoto et al., 2016). Parameter δ (m) in equation 10 denotes the viscous sublayer thickness, or the near-surface region of the aboveground atmospheric turbulent boundary layer in which momentum transfer is dominated by viscous forces (Schlichting & Gersten, 2017); this value can be estimated from experimental data (e.g., Cebeci & Smith, 1974; Pope, 2000) or surface renewal theory (e.g., Komori et al., 1989; Meek & Baer, 1970). A discussion of the determination of this variable from the data sets of Trautz et al. (2018) can be found in section 3.1. The term $f(\theta_{surf})$ is a surface wetness-dependent function expressed as (Haghighi & Or, 2013; Schlünder, 1988)

$$f(\theta_{surf}) = \frac{1}{\pi\sqrt{\theta_{surf}}}\left(\sqrt{\frac{\pi}{4\theta_{surf}}}-1\right), \quad (11)$$

The thermal boundary condition along the top of the model domain is specified in terms of a sensible heat flux H (W/m^2) expressed as

$$J_H = H = -h[T - T_a(t)], \quad (12)$$

where T (K) is the surface temperature calculated by the model and T_a (K) is the time-dependent air temperature measured immediately outside of the viscous sublayer. As experimental studies have shown that temperature gradients are linear across the viscous sublayer (Gaikovich, 2000), and in keeping with the approach used to define the evaporative flux, the heat transfer coefficient h (W·m^{-2}·K^{-1}) in equation 12 is formulated as

$$h = \frac{\lambda_a}{\delta}, \quad (13)$$

where λ_a (≈0.024 W·m^{-1}·K^{-1}) is the thermal conductivity of air and δ (m) is the experimentally measured viscous sublayer thickness.

2.2.4 Numerical Methods

The numerical solution of the coupled partial differential equations (equations 1a, 1b, 3, and 6) for the different scenarios described in section 2.3 was obtained with the commercial software, COMSOL Multiphysics environment. The Galerkin finite element method with a quadratic spatial-discretization scheme for Lagrange triangular elements was employed. The built-in PARDISO direct solver based on LU decomposition was employed to solve the system matrix. This solver is fully coupled in that it operates on the full Jacobian matrix and includes the couplings between all of the unknown variables. PARDISO was selected over other available solvers for its ability to handle large, sparse, nonsymmetric linear systems of equations and its ability to store the solution out-of-core, reducing computational memory requirements. Time was advanced using the implicit backward Euler method with an adaptive time-stepping scheme relying on a damped Newton solver to aid in convergence of this highly nonlinear problem. The triangular mesh composed of nominally 5-mm edge lengths (refined locally at the soil surface to 0.5–1 mm, depending on experimental scenario) was determined through

a mesh convergence analysis that focused on solution stability and overall effect of mesh size on the calculated evaporative water losses; the mesh was continuously refined until changes in water loss no longer exceeded an arbitrary determined threshold of 10^{-6} kg. The model was calibrated a priori using training data sets generated by Trautz (2015) in the same experimental system as Trautz et al. (2018) and soil properties (e.g., van Genuchten parameters) measured in small, effectively one-dimensional column drainage experiments. After this initial calibration, no additional fitting was performed during the numerical simulations.

2.3 Numerical Experiments

The numerical experiments outlined below explore the sensitivity of the porous media heat and mass transfer model described in the preceding section to the spatial-discretization length-scales over which atmospheric forcing data are averaged and provided as inputs. The design of the numerical experiments was based on the traditional adage that the provision of more information to a model will improve the accuracy and realism of simulation results. In the context of the present study, one can therefore hypothesize that shorter atmospheric forcing spatial-discretization length-scales will better capture the local soil-atmosphere feedback affecting the subsurface state. The question that must be asked pertains to the spatial resolution, or amount of forcing data (i.e., spatial resolution), that needs to be provided to the model to adequately capture evaporative water losses and the spatial distributions of soil moisture and temperature—these findings can in turn be used to inform future experimental data collection strategies. Borrowing from Albertson and Parlange (1999) who investigated the impact of horizontal surface roughness variability on land-atmosphere momentum exchanges and feedback, “to begin to develop a general answer to [such] questions demands a vast amount of information describing surface fluxes distributed in space and time over the study area and the dynamics of interaction between the surface and the atmospheric motions.” The present study addresses this particular issue by using the large-scale (7.15 m long), high-resolution bare-soil evaporation experimental data sets generated by Trautz et al. (2018) under carefully prescribed climatic and edaphic conditions in a low-wind speed, climate-controlled micrometeorological wind tunnel coupled to a soil tank at the Center for Experimental Study of Subsurface Environmental Processes in Golden, Colorado.

Following the work of Trautz et al. (2018), a series of four scenarios are considered herein (Figure 1). These scenarios, hereon denoted EX-1 through EX-4, are distinguishable in terms of the applied soil packing configuration and surface roughness; wind speed, air temperature, and relative humidity were held constant among the scenarios at values of 0.8 m/s, 23.8 °C, and 22%, respectively. The edaphic conditions were varied to induce different soil-atmosphere coupling scenarios in which different aboveground and belowground flow and transport phenomena would dominate (Trautz et al., 2018). In this study, Scenario EX-1 consists of a flat homogeneous packing

configuration, EX-2 consists of a flat heterogeneous packing configuration, EX-3 consists of an undulating homogeneous packing configuration, and EX-4 consists of an undulating heterogeneous packing configuration.

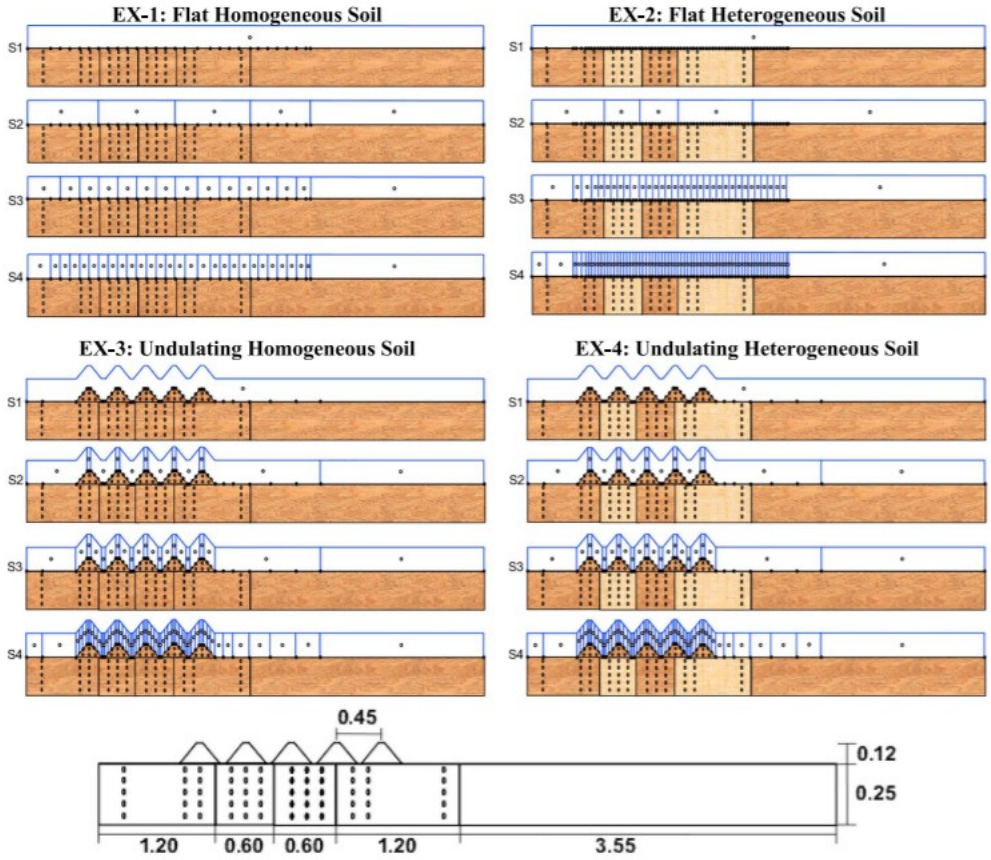

Figure 1. Depiction of the four experimental scenarios of Trautz et al. (2018) and spatial-discretization (blue rectangles) scheme used to average the atmospheric forcing data sets during each model simulation. Brown denotes the coarse-textured sand and tan, the fine-textured sand. All dimensions given in meters and atmospheric flow occur from right to left in the images.

A model domain with dimensions and soil properties identical to those used in Trautz et al. (2018) was created for each experimental scenario (Figure 1). Note that the soil tank used in the experiments of Trautz et al. (2018) had physical dimensions of l × *d* × *w*:7.15 × 1.1 × 0.11 m. The homogeneous packing configurations of EX-1 and EX-3 were composed of a coarse-textured sand (Granusil #30) while the heterogeneous packing configurations in EX-2 and EX-4 were composed of alternating layers of coarse- (Granusil #30) and fine-textured sand (Accusand #50/70; see Figure 1). A summary of the key physical, hydraulic, and thermal properties of these sands assigned to the model are provided in Table 1. Surface roughness was defined in the scenarios as either being flat (EX-1 and EX-2) or in the case of EX-3 and EX-4, a series of five trapezoidal undulations (Figure 1).

Table 1
Summary Physical, Hydraulic, and Thermal Properties of Test Soils Used in Trautz et al. (2018)

Soil Properties[a]

Sand	d_{50} (cm)	Porosity (m^3/m^3)	Residual Water Content (m^3/m^3)	Intrinsic Permeability (cm^2)	Air Entry Head (cm)	Saturated Hydraulic Conductivity (cm/s)	Saturated Thermal Conductivity ($W \cdot m^{-1} \cdot K^{-1}$)
#30	0.050	0.42	0.027	2.26×10^{-6}	16.6	0.116	2.97
#50/70	0.027	0.40	0.033	2.96×10^{-7}	34.1	0.029	2.84

Model constitutive equation parameters[b]

Sand	van Genuchten parameters		Phase change coefficient
	α (cm^{-1})	n (–)	b (s/m^2)
#30	0.071	15.68	7.5×10^{-5}
#50/70	0.039	10.23	2.0×10^{-5}

[a]Illangasekare et al. (1995), Schroth et al. (1996), Sakaki and Illangasekare (2007), and Sakaki et al. (2013) [b]Sakaki and Illangasekare (2007) and Trautz et al. (2015)

Prior to the start of the experiments, the top boundary of the model domain (i.e., the soil surface) was divided into smaller intervals (not to be confused with the models mesh created afterward) over which atmospheric forcing data would be applied (see Figure 1). The total number of intervals defined along this boundary was based on the number atmospheric velocity and relative humidity/temperature profiles measured by Trautz et al. (2018); the locations of these intervals were centered around the physical measurements. The numerical experiments of the present study were designed as a series of four simulations (denoted S1, S2, S3, and S4) that were run for each edaphic scenario. In each simulation of a given scenario, the associated atmospheric forcing data set was divided into a different number of “longitudinal (streamwise) averaging intervals” as depicted in Figure 1 and summarized in Table 2. The atmospheric measurements located within a defined interval were averaged together and provided as the forcing input to all corresponding boundary intervals (Figure 1); note that a weighted mean was calculated in order to account for the spacing distance between the measurements in an input interval. The use of averaged values, rather than a randomly selected measurement within a spatial-discretization length interval, was designed to help reduce any temporal climate control variability (±3% relative humidity, ±1 °C temperature) associated with the wind tunnel that could bias a single data point taken within the 6- to 8-hr experimental measurement window (Trautz et al., 2018). The definition of a different number of input intervals in each simulation created different spatial-discretization length-scales that were used to force the model (Table 2). As depicted in Table 2, the spatial-discretization length-scales over which the atmospheric forcing data were averaged decreased from simulation S1 (7.15 m) to simulation S4 (0.059–0.153 m). This sequential reduction in the spatial-discretization length-scale was designed to specifically allow the hypothesis introduced above to be tested. When rephrased here in the context of these experiments, one can posit that if the model is sensitive to spatial variations in atmospheric conditions, the accuracy and realism of simulations should improve as spatial-discretization length-scales are reduced from simulation S1 to S4.

Table 2
Applied Spatial Discretization of Atmospheric Forcing Data

	Simulation S1		Simulation S2		Simulation S3		Simulation S4	
Experiment	Number Averaging Intervals	Mean Averaging Length (m)	Number Averaging Intervals	Mean Averaging Length[a] (m)	Number Averaging Intervals	Mean Averaging Length[a] (m)	Number Averaging Intervals	Mean Averaging Length[a] (m)
EX-1	1	7.15	5	1.125	15	0.302	29	0.153
EX-2	1	7.15	5	0.90	35	0.118	69	0.059
EX-3	1	7.15	12	0.301	22	0.158	56	0.065
EX-4	1	7.15	12	0.301	22	0.158	56	0.065

[a]Calculation of mean averaging length excludes first upstream interval

3 Results and Discussion

In this section the spatiotemporal variability of the measured atmospheric forcing data of Trautz et al. (2018) are discussed for the four experimental scenarios. This is followed by a detailed discourse focused on the impacts of the spatial-discretization length-scale over which atmospheric data are averaged and provided to force the model; results are analyzed in the context of mass transfer (i.e., soil moisture redistribution and cumulative evaporative water loss) and heat transfer (i.e., soil temperature distribution).

3.1 Model Inputs

Wind velocity and relative humidity/air temperature (RHT) profiles were measured by Trautz et al. (2018) in the wind tunnel test section along the 7.15-m length of the soil tank between the heights of 0.5 and 40 cm using laser Doppler velocimetry and a custom-made relative humidity/temperature sensor. These measurements resulted in the generation of data sets consisting 400 to 700 individual point measurements per atmospheric variable; the total number of measurements varied between experiments in response to the complexity of the applied packing configuration and surface roughness. As will be demonstrated below, out of all these available measurements, only those closest to the soil surface were used; all spatial averaging was therefore conducted solely in the longitudinal direction. Given the large size of these data sets, extensive postprocessing was required with respect to determining the thickness of the viscous sublayer and selecting appropriate air temperature and relative humidity data points to be provided to the model.

The thickness of the viscous sublayer that forms above a surface in the presence of airflow varies from location to location in response to local changes in velocity and turbulence (Pope, 2000). The thickness of the viscous sublayer was estimated along the length of the soil tank using near-surface velocity profile measurements (e.g., Figure 2a) and the self-similar logarithmic law of the wall for turbulent flow (Schlichting & Gersten, 2017). According to the law of the wall, the viscous sublayer is defined as the region of a turbulent boundary layer that is located below 5 dimensionless wall coordinate units:

$$z^+ = \frac{z u_*}{\nu}, \quad (14)$$

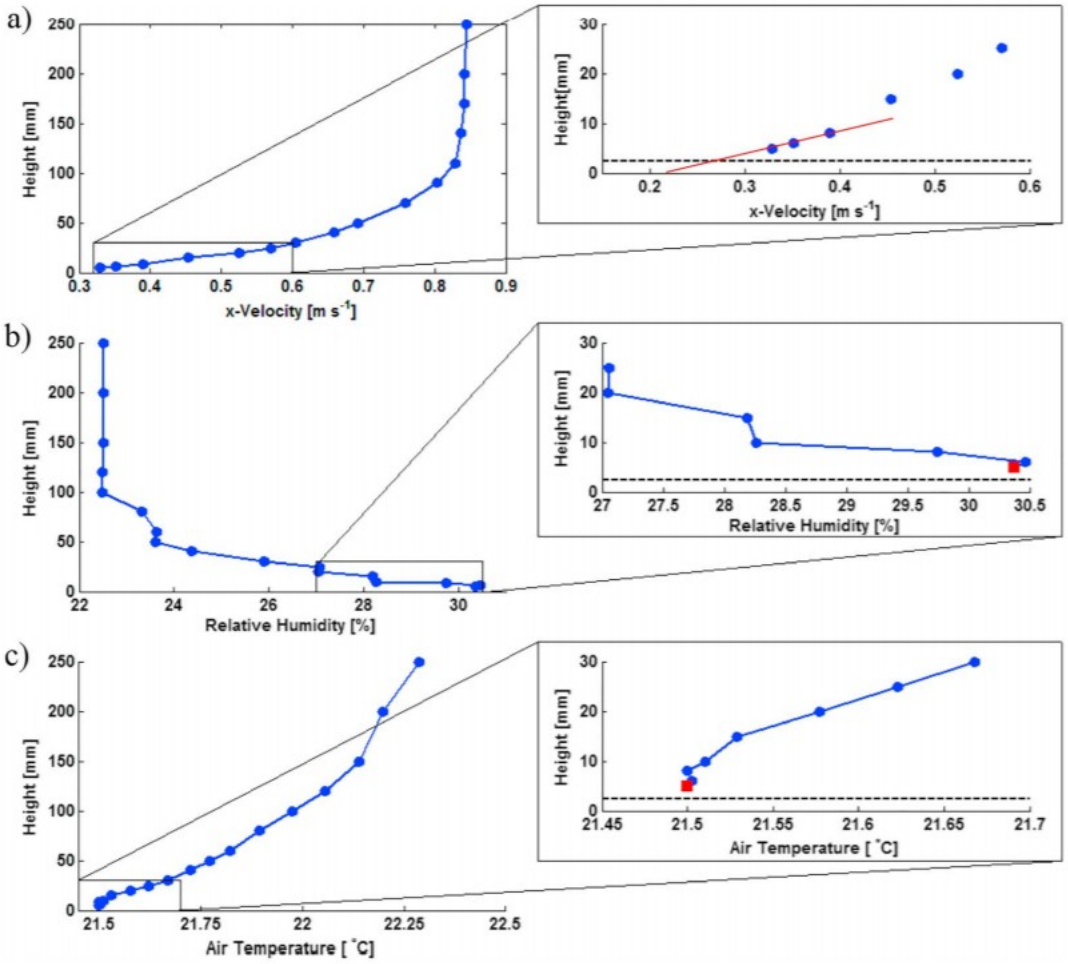

Figure 2. An example of a local (a) velocity profile, (b) relative humidity profile, and (c) air temperature profile measured above the soil surface. The red line in (a) denotes the extrapolated velocity profile to the soil surface. The black dashed line demarcates the estimated outer boundary (i.e., thickness) of the viscous sublayer. The red squares denote the closest available relative humidity/temperature measurement to the viscous sublayer used in the prescribed boundary condition. All data shown were measured at a specific distance during EX-1 ($x = -520$ cm; see Figures 3 and 4).

where z (m) is the height and ν (m^2/s) is the kinematic viscosity. The term u_* (m/s) is the friction or shear velocity expressed as (Pope, 2000)

$$u_* = \sqrt{\frac{\tau_w}{\rho}}, \quad (15)$$

where τ_w (Pa) is the local fluid wall stress calculated according to

$$\tau_w \equiv \tau(z = 0) = \mu \left.\frac{\partial u}{\partial z}\right|_{z=0}. \quad (16)$$

Combining and rearranging equations 14–16 and setting $z^+ = 5$ yields an estimated local viscous sublayer thickness δ (m), of

$$\delta = z = 5\sqrt{\nu \frac{\Delta z}{\Delta u}}. \quad (17)$$

Velocity measurements could not be taken at distances less than 5 mm above the soil surface as a result of laser system and wind tunnel test-section physical limitations. The velocity gradient present in equation 17 was therefore determined extrapolating the measured profile to the soil surface (see the red line in Figure 2a).

Figure 3 displays the final viscous sublayer thickness estimated along the length of the soil tank for the four experimental scenarios of Trautz et al. (2018). Parameter δ showed the greatest stability in the case of the flat soil surface experimental scenarios (i.e., EX-1 and EX-2), deviating by less than 0.2 mm from the mean value of 2.3 mm along the entire length of the soil tank. Significant variations in δ could be observed in EX-3 and EX-4 in which the surface undulations were present however. In these experiments, the thickness of the viscous sublayer was close to that observed in EX-1 and EX-2 upstream of the surface undulations. As the flow encountered the surface undulations, the local fluid dynamics changed leading to significant variations in the viscous sublayer thickness. Parameter δ increased above the upstream face of the first undulation as the flow accelerated and moved vertically away from the soil surface (see Figure 4; Trautz et al., 2018). This flow acceleration, a phenomenon referred to as speed-up (e.g., Jackson & Hunt, 1975), was also responsible for the viscous sublayer thinning observed at the crest of each undulation. The thickening and thinning of the viscous sublayer above the downstream and upstream faces of the subsequent undulations were, respectively, caused by flow separation and reattachment (Haghighi & Or, 2015a; McInnes et al., 1994; Trautz et al., 2018).

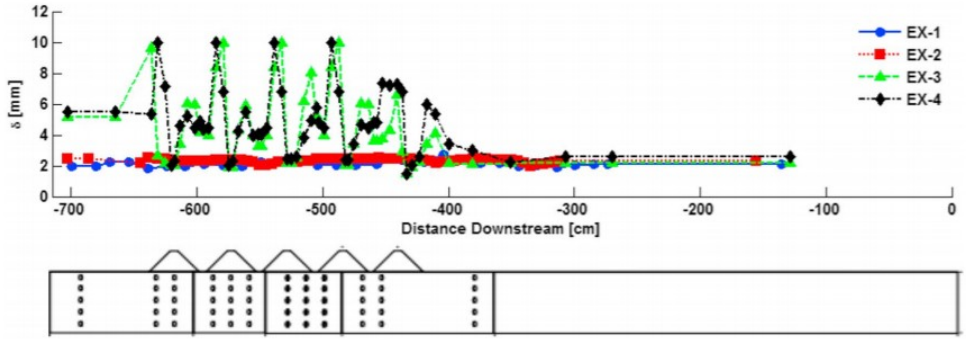

Figure 3. Viscous sublayer thickness along the length of the soil tank estimated from experimental velocity measurements of Trautz et al. (2018) for the four experimental scenarios. Note that atmospheric airflow occurs from right to left (i.e., 0 to −715 cm). Schematic provided denotes the locations of surface undulations and soil layers.

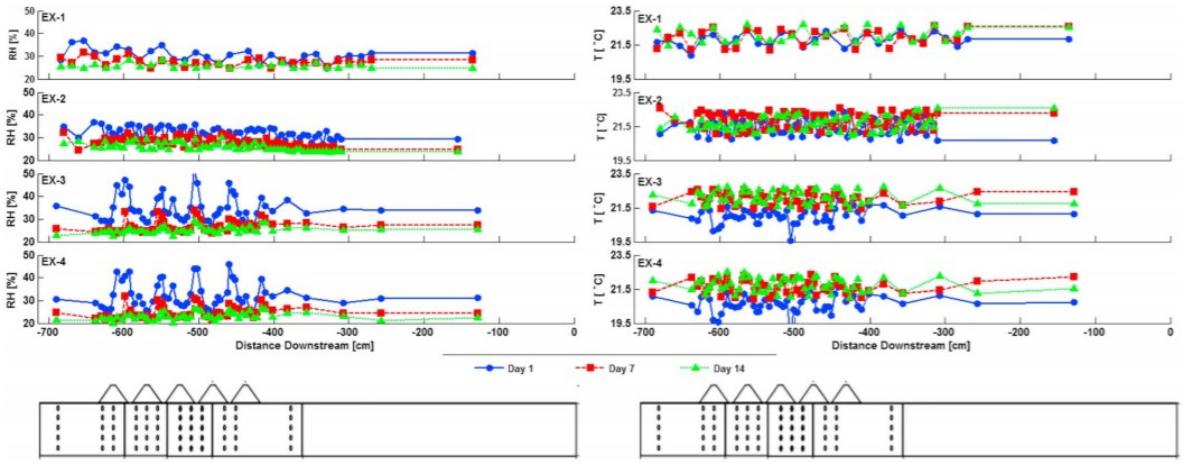

Figure 4. Spatiotemporal distributions of relative humidity and air temperature measured immediately outside the viscous sublayer corresponding to the inputs provided to the model during simulation S4 for each experimental scenario. Note that atmospheric airflow occurs from right to left (i.e., 0 to −715 cm). Schematics provided denote the locations of the surface undulations and soil layers.

In addition to being used directly in the model boundary condition formulation (equations 10 and 13), the thickness of the viscous sublayer was critical to the selection of the relative humidity and temperature inputs. This selection process simply involved identifying the RHT measurement data point made at the height closest to δ within a given profile (Figures 2b and 2c) to best represent conditions immediately outside the viscous sublayer. Figure 4 presents the spatial distribution of relative humidity and air temperature measured outside of the viscous sublayer on days 1, 7, and 14 of the four experiments over a 6- to 8-hr time period (Trautz et al., 2018). Each measurement data set was applied as a constant forcing input for the week between available measurements. The results show that each experiment displayed the same general temporal behavior—a decrease in average relative humidity and an increase in average air temperature with time. These trends corresponded to the associated reduction in evaporation rates as the soil transitioned from Stage I to Stage II evaporation.

Inspection of Figure 4 reveals that at early times, day 1 in particular, quantifiable macroscopic trends in relative humidity and air temperature that may impact the simulated soil moisture and temperature distribution could be observed. The macroscopic spatial variability or longitudinal trends in the RHT measurements (Figure 4) can be interpreted in terms of airflow and the applied edaphic conditions. In the case of the two flat soil surface experiments (i.e., EX-1 and EX-2), a unique airflow-dependent micrometeorological phenomenon referred to as the fetch effect (i.e., an occurrence of larger upstream evaporation than downstream as a result of elevated relative humidity and lower air temperatures with distance downstream) contributed to the elevated relative humidity values measured above the downstream portion of the soil tank (Castellví, 2012; Horst & Weil, 1994); air temperature did not display the same longitudinal spatial sensitivity.

The surface undulations present in EX-3 and EX-4 also had a visible impact on the near-surface RHT spatial distributions (Figure 4). The highest relative humidity values and coolest temperatures were observed in the troughs between the surface undulations; the driest and warmest conditions were subsequently measured above the crests of the surface undulations. These trends can be explained in terms of a combination of local differences in the airflow dynamics (flow recirculation versus speed-up) and evaporation behavior (Stage I versus Stage II evaporation) that result from the presence of the surface undulations (Veihmeyer, 1938; McInnes et al., 1994; Wagner et al., 2011); the reader is referred to Trautz et al. (2018) for a detailed discussion.

3.2 Mass Transfer

Soil moisture distributions measured and simulated on day 3 are presented in Figure 5 for the four experimental scenarios tested. The reader is referred to Trautz et al. (2018) for a detailed analysis of the experimental results in the context of mass transfer. Given the complimentary nature of this work to that of to Trautz et al. (2018), focus is given herein to the analysis of day 3 soil moisture distributions that are furthermore representative of Stage I evaporation which as discussed earlier, is primarily influenced by atmospheric conditions (i.e., wind speed, air temperature, relative humidity, solar radiation). One can therefore expect that the model should show the greatest sensitivity to the applied atmospheric forcing data at this time. Note that analysis of the results is furthermore constrained to the downstream 3.6-m extent of the soil tank/model domain where the edaphic features were created, and greatest number of atmospheric measurements were taken.

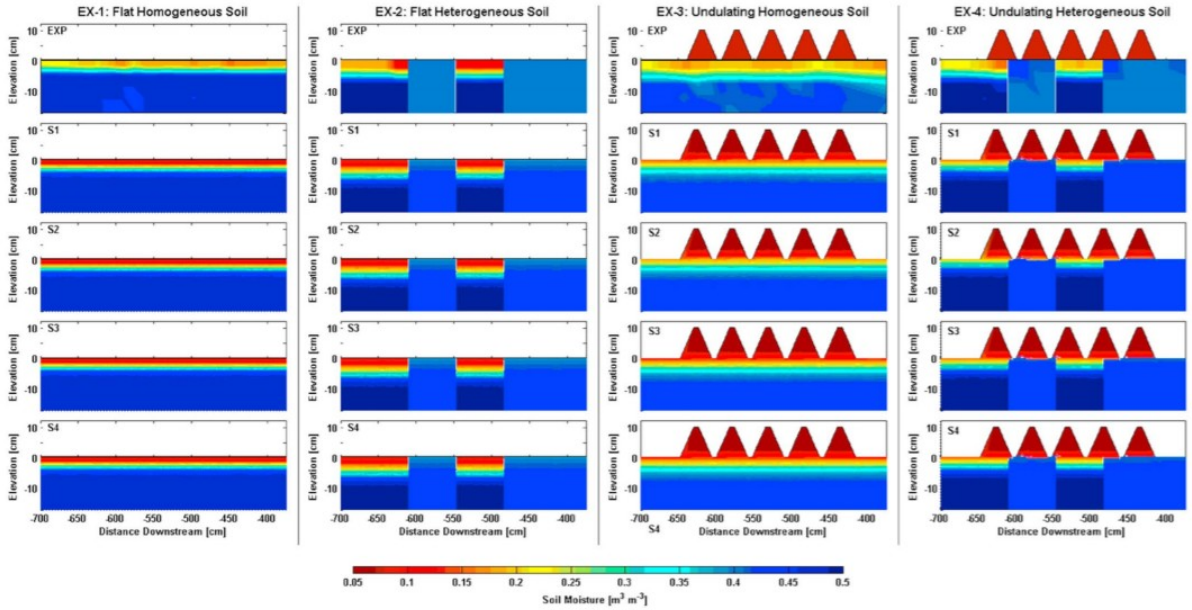

Figure 5. Day 3 soil moisture distributions for the four experimental scenarios tested in Trautz et al. (2018). For each scenario, the top surface plot corresponds to interpolated experimental measurements and each subsequent surface plot below, the simulated distribution at decreasing spatial-discretization length-scale. Atmospheric flow occurs from right to left in each surface plot (i.e., 0 to −715 cm).

Soil moisture measured during EX-1 within the top 5 cm of the soil varied by a maximum of 0.05 m^3/m^3 along the 3.5-m downstream extent of the soil tank as shown in Figure 5. This correlates well with the observed increase in relative humidity over the same distance (see Figure 4), suggesting that the atmospheric feedback associated with the fetch effect (i.e., 10% difference in upstream and downstream relative humidity) are sufficiently strong so as to impact the shallow soil moisture dynamics during Stage I evaporation. The simulation result for EX-1 does show this trend, albeit to a considerably smaller degree. Soil moisture simulated at a depth of 2.5 cm showed a longitudinal variation of less than 0.3% among the four simulations over the 3.5-m downstream extent of the model domain; the evaporative fluxes similarly varied by less than 5×10^{-4} $kg \cdot m^{-2} \cdot s^{-1}$ over this same distance. This lack of sensitivity to local changes in the atmospheric demand associated with the applied spatial discretization length-scale, resulted in a drying depth consistent with that observed experimentally but an overprediction of the rate or, total amount of soil drying occurring within the first three days of the experiment.

The soil moisture distributions for the flat heterogeneous soil experimental scenario (EX-2) again demonstrate little sensitivity to the applied spatial-discretization length-scale. Soil moisture varied horizontally by less than 0.3% at a depth of 2.5 cm within a given sand layer. The longitudinal variability in soil moisture depicted between the different soil layers in EX-2 can be attributed to differences in soil properties and drying rates. The lack of sensitivity to applied forcing data may be attributed in part to the presence of a secondary co-occurring and dominant transport phenomenon referred to as capillary pumping. This phenomenon transported soil water from the hydraulically connected coarse-textured soil layers to the fine-textured-soil layers as a result of a capillary head gradient (Lehmann & Or, 2009; Yiotis et al., 2001).

The surface undulations of EX-3 and EX-4 created unique soil moisture patterns (Figure 5) because the surface undulations provided greater resistance to water vapor transport by increasing the average effective water vapor diffusion pathway length and creating local differences in the microclimate (Holmes et al., 1960; Willis & Bond, 1971). As discussed in Trautz et al. (2018), these surface undulations affect the vapor transport in a similar manner to that of vapor barriers or mulch layers. The simulation results depicted in Figure 5 for these two experimental scenarios also displayed elevated soil moisture (~0.07 m^3/m^3) near the base of the surface undulations, something that could not be captured by the low-resolution sensor networks employed in Trautz et al. (2018).

Although it difficult to discern from inspecting Figure 5, the simulated near-surface soil moisture was significantly more sensitive to the spatial-discretization length-scale of the atmospheric forcing data when the soil surface undulations were present (EX-3 and EX-4). Table 3 shows that as in the case of the flat soil surface experiments, there is very little longitudinal

spatial variability within the top 2.5 cm of the soil. The model displays hydrostatic drying behavior and fails to capture the ~2–3% local variability observed experimentally beneath the series of undulations. Average soil moisture was observed to decrease as the spatial resolution of the atmospheric forcing data points were increased from simulations S1–2 to simulations S3–4 and the impact of the spatial averaging of the forcing data became less pronounced. This decrease corresponded directly to a larger number of boundary "averaging intervals" being provided input values consisting of smaller δ values and higher atmospheric demand (i.e., lower relative humidity, higher temperature); the thinner local viscous sublayer thicknesses reduced the boundary layer resistance (equation 10) and the higher atmospheric demand increased the vapor density and thermal gradients (equations 9 and 12).

Table 3
Average Soil Moisture Values Simulated on Day 3 of EX-3

	Location Relative to Surface Undulations		
Simulation Number	Upstream	Below Undulation	Below Trough
EXP	0.177	0.183	0.205
S1	0.246	0.248	0.249
S2	0.273	0.270	0.272
S3	0.215	0.213	0.214
S4	0.217	0.215	0.216

These findings suggest that as the scale of the surface roughness increases, as in the case of EX-1 and EX-3, the effects on the local microclimate become more pronounced and important—justifying the use of smaller discretization length-scales. Despite significant local differences in forcing conditions (Figures 3 and 4), the values displayed in Table 3 show that the soil moisture distribution was not sensitive to the applied spatial-discretization length-scale. As shown in Figure 6 which presents time-dependent cumulative water losses measured and simulated for the four experimental scenarios however, there is a discernable and quantifiable effect on the drying behavior (i.e., evaporative cumulative water loss). Cumulative water loss was determined through a two-dimensional integration of the soil moisture data across the model domain at each model output time step:

$$WL = \iint w\rho_l(\phi - \theta_l)d\Omega, \quad (18)$$

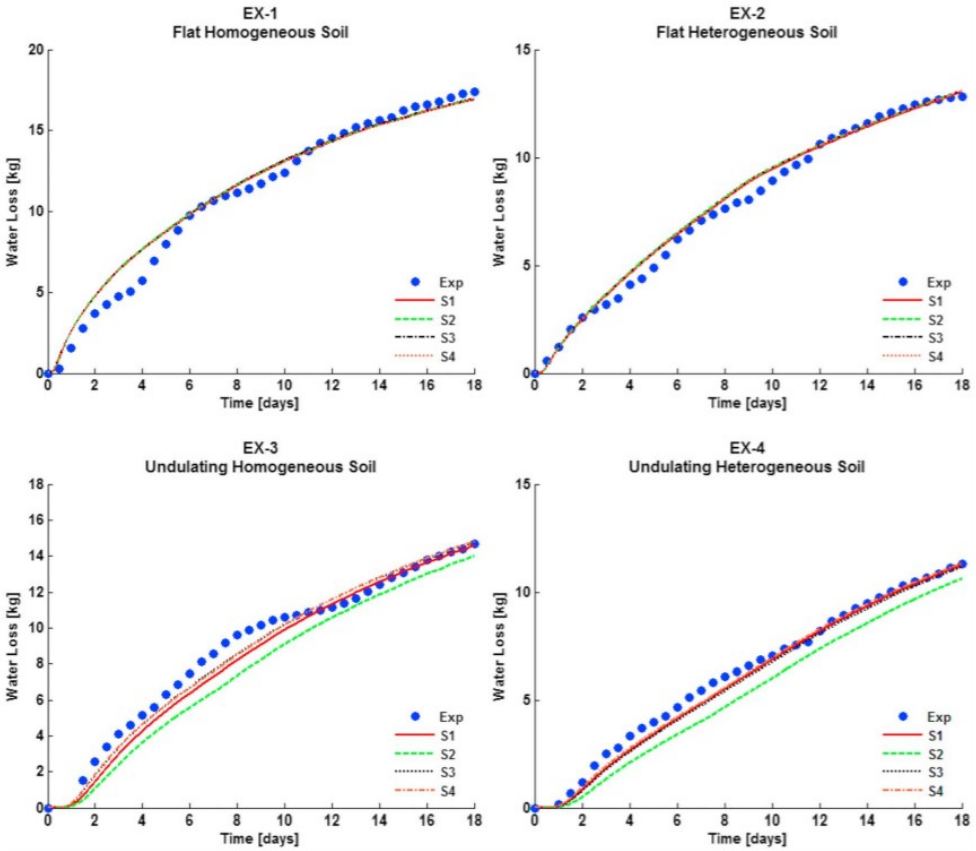

Figure 6. Experimentally measured and simulated time-dependent cumulative evaporative water loss determined over the downstream 3.5-m extent of the soil tank for the four experimental scenarios of Trautz et al. (2018).

where w (m) is the width of the soil tank in Trautz et al. (2018), ρ_l (kg/m^3) is the density of water, ϕ (m^3/m^3) is the soil porosity, and θ_l ($=S_l\phi$; m^3/m^3) is the water content. The surface undulations were excluded from the calculations in EX-3 and EX-4 as soil moisture could not be measured at sufficiently high resolutions in Trautz et al. (2018) to perform accurate mass balances.

Visual inspection of Figure 6 demonstrates that the model is able to capture both the behavior (i.e., shape) and magnitude of cumulative evaporative water losses with great accuracy—confirmed statistically in Table 4. As in the case of soil moisture, the model showed little sensitivity to the applied spatial-discretization length-scale of the forcing data in terms of impacts on cumulative evaporative water loss in the two flat soil scenarios. Comparison of the measured and simulated water loss curves reveals that the model's failure to capture the asymmetric drying patterns induced by the fetch effect in EX-1 and capillary pumping in EX-2 had little meaningful impact. The cumulative evaporative water loss curves for the two undulating soil surface experiments (Figure 6) on the other hand do show sensitivity to the applied forcing data spatial-discretization length-scale. The best prediction of the experimentally measured water loss curves occurred in the case of simulation S4 in which the greatest number of atmospheric forcing data points. Simulation S2 provided the worst fit of the experimental water loss

curves, underestimating the final water losses in EX-3 and EX-4 by 0.8 and 0.6 kg, respectively. This poor fit is not entirely unexpected as simulation S2 applied atmospheric forcing data with a 1 °C cooler averaged air temperature, 12–15% higher averaged relative humidity, and 2–3-mm thicker averaged viscous sublayer over the majority of the surface boundary intervals than any of other three simulations.

Table 4
Coefficients of Determination of Simulated Cumulative Evaporative Water Loss

Experiment	S1	S2	S3	S4
EX-1 (flat homogeneous soil)	0.9808	0.9800	0.9807	0.9808
EX-2 (flat heterogeneous soil)	0.9920	0.9905	0.9912	0.9913
EX-3 (undulating homogeneous soil)	0.9741	0.9210	0.9850	0.9856
EX-4 (undulating heterogeneous soil)	0.9908	0.9335	0.9874	0.9935

3.3 Heat Transfer

Figure 7 depicts soil temperature distributions measured and simulated on day 3 of the four experimental scenarios described above; day 3 is again chosen for analysis as conditions are representative of atmospheric demand-controlled Stage I evaporation. Figure 7 shows that the simulations are able to capture the experimentally measured trends in soil temperature; however, the temperature was consistently overestimated within the first 5 cm and the total depth to which the atmospheric feedback signal propagated underestimated. Temperature increased with depth in the physical experiments and simulations as the soil's ability to store heat and resist changes in temperature (i.e., effective volumetric heat capacity) as a result of increases in soil moisture—increasing nonlinearly with water content (Berge, 1990; Prunty & Horton, 1994). The coolest temperatures were observed closest to the soil surface where in the first several centimeters, the temperature was suppressed by evaporative cooling (Monteith, 1981; Yiotis et al., 2007) and convective cooling (Haghighi & Or, 2015b; Hanks et al., 1967).

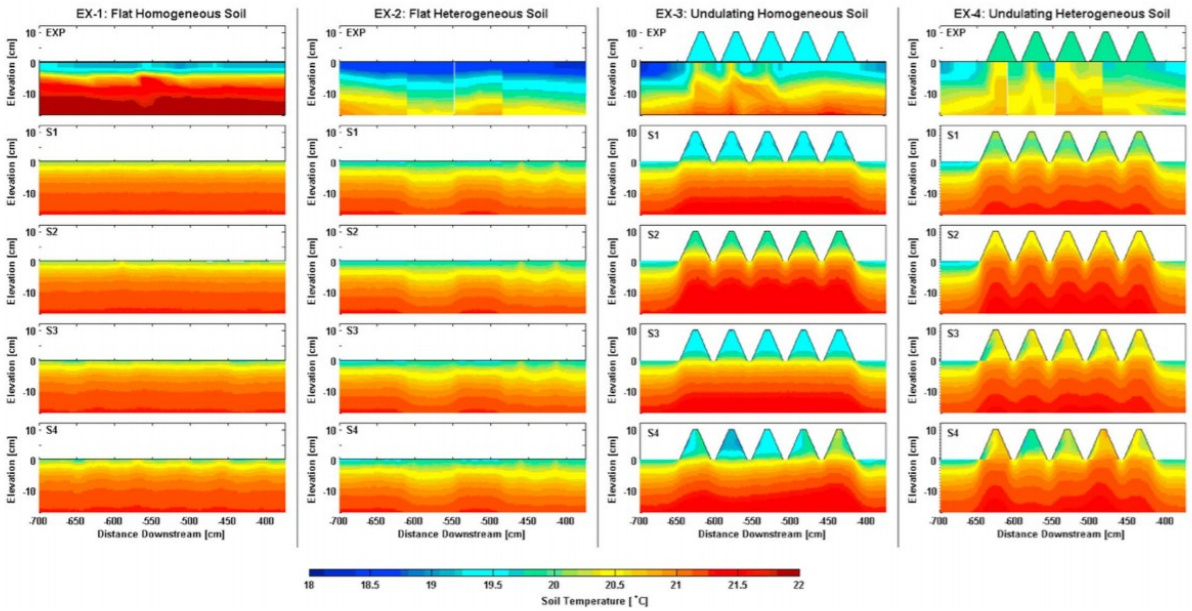

Figure 7. Day 3 soil temperature distributions for the four experimental scenarios tested in Trautz et al. (2018). For each scenario, the top surface plot corresponds to interpolated experimental measurements and each subsequent surface plot below, the simulated distribution at decreasing spatial-discretization length-scale. Atmospheric flow occurs from right to left in each surface plot.

Unlike soil moisture, horizontal variations in simulated soil temperature could be observed along the length of the model domain in all four experimental scenarios. In the case of experiment EX-1, simulations S3 and S4 showed cyclical patterning air temperature distribution shown in Figure 4; the coolest soil temperatures were observed beneath the boundary intervals in which the coolest air temperature data were applied. Variations in soil temperature were also visible in the flat heterogeneous soil experiment (EX-2) simulations, constrained in this case to the individual soil layers with the coolest temperatures penetrating to the greatest depths in the fine-textured fully saturated layers (Figure 7). The failure of the model to capture the same degree of cooling in the first 5 cm can be attributed primarily to the heat transfer physics included in the applied thermal boundary condition parameterization—the model currently only accounts for heat diffusion across the viscous sublayer (i.e., sensible heat flux component).

Unique soil temperature distributions which followed the shape of the surface undulations could be observed in EX-3 and EX-4. The coolest temperatures were observed upstream and downstream of the surface undulations; the surface undulations dampened the effect of the atmospheric temperature on the main soil body. In the immediate vicinity of the surface undulations, the coolest temperatures were locally observed beneath the troughs where the cooler air temperature forcing data were directly applied. As in the case of soil moisture, the model's ability to capture trends that could not be measured by Trautz et al. (2018) within the surface undulations could be discerned. The surface undulations displayed a uniform soil temperature in simulation S1 where a single air temperature value was applied across the

top boundary of the model. As the resolution of the input files increased (i.e., spatial-discretization length-scale decreased), greater soil temperature variability was observed within the surface undulations. In simulations S3 and S4, the coolest temperatures were observed along the downstream face of the undulations where the lowest air temperatures were applied.

4 Discussion and Outlook

In this study, the sensitivity of a REV-scale coupled heat and mass transfer porous media model to the spatial-discretization length-scale of applied atmospheric forcing data was tested. As discussed earlier, this work was inspired by observed horizontal variations in the near-surface soil moisture and soil temperature distributions observed by Trautz et al. (2018) in a series of wind tunnel experiments. One of the primary objectives of this investigation was to use these findings to explore the resolution of the atmospheric data (e.g., air temperature, relative humidity, wind speed) that needs to be collected and provided to force a model (at a 1–10-m length-scale) to accurately simulate water loss and soil moisture/temperature patterns in initially saturated sandy soils exposed to strictly drying conditions. Being able to adequately capture subsurface soil moisture and temperature dynamics with a minimal amount of forcing data or large spatial-discretization length-scales is desirable from both an experimental and computational stand point; high-resolution data sets are costly from a monetary and time stand point to generate, take significantly longer to postprocess, and can be more computationally intensive to use.

The simulated soil moisture distributions for the four experimental scenarios in this study consistently showed little to no sensitivity to the spatial-discretization length-scale of the atmospheric forcing data used to force the model. The corresponding longitudinal variability in the observed atmospheric forcing conditions (Figures 3 and 4) were not strong enough to produce the same effect as those observed in Trautz et al. (2018) in the simulated local soil moisture distributions; a slight impact on the soil temperature (Figures 5 and 7) was observed however. Despite the model's inability to capture these small, and depending on the simulation objectives, possibly negligible details, results demonstrated that this had little bearing from a water balance perspective. Evaporative water losses from the main soil body could be simulated with great accuracy using minimal atmospheric forcing data—an important caveat being the selection of atmospheric measurements used to force the model. The results presented in Figure 6 demonstrates that for more complex surface conditions of EX-3 and EX-4, simulated water loss could be either overestimated or underpredicted based on any microclimatic bias introduced by the location where the applied inputs were measured experimentally. In such scenarios, there is enough variability in measurements between the peak and valleys of the surface undulations (8 mm δ, 10–15% RH, and 1–2 °C T) to have a statistically significant impact (Table 4) on simulated water loss. The use of measurements made in the cooler and moister valleys between the surface

undulations in simulation S2, for example, resulted in the worst fit which underestimated water loss by approximately 1 kg by the end of the simulation.

Collectively, these results demonstrate that there is no need to generate high-resolution atmospheric data sets for the experimental conditions of Trautz et al. (2018), which consisted of a sandy soil with a either a flat surface or surface consisting of a uniform series of undulations. While perhaps not fully realized because of the design of the surface undulation experiments of Trautz et al. (2018) which together behave like a vapor barrier, these results do suggest that the generation of high-resolution data sets and use of small model spatial discretization-length scales may still be important under certain circumstances. Complex surface conditions with large-scale surface roughness or discrete objects (e.g., vegetation, buildings, single mounds) can provide significant flow obstruction, changing the coupling strength between soils and the atmosphere (manifested through near-surface microclimate variability) as well as the governing heat and mass transfer physics of the system. Under strong coupling conditions such as those proposed above, it may be possible to better capture longitudinal soil moisture and soil temperature variability as the feedback between the two systems becomes more apparent and influential (Trautz, Illangasekare, & Rodriguez-Iturbe, 2017; Trautz, Illangasekare, Rodriguez-Iturbe, Heck, & Helmig, 2017); this is a topic warranting further investigation.

Given the general insensitivity of the model to the applied spatial discretization length-scale for the experimental scenarios tested herein, the findings suggest that greater experimental and modeling time and effort should be spent characterizing the soil and exploring model methodologies/parameterizations than generating high spatial-resolution atmospheric data sets such as those of Trautz et al. (2018). This consideration is addressed briefly in two additional final numerical experiments presented in Figure 8: the first focusing on soil heterogeneity and the second, the prescribed boundary condition parameterization.

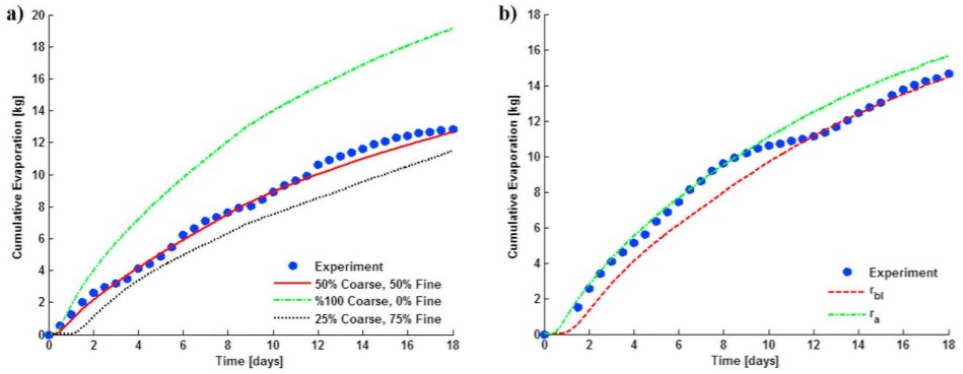

Figure 8. Simulated cumulative evaporative water loss curves demonstrating that greater time and effort should be devoted to characterizing soil conditions in the context of (a) soil heterogeneity and (b) microtopographic features than the generation of high-resolution atmospheric forcing data sets. The proportion of the volume of coarse- and fine-textured soils were varied in (a) and the surface undulations described with a roughness term in an atmospheric resistance formulation in (b).

In the first experiment (Figure 8a), the soil heterogeneity of EX-2 was replaced with two different vertical packing configurations consisting of (1) 100% coarse- and 0% fine-textured soil and 2 75% coarse- and 25% fine-textured soil. In these simulations the model was forced with the same atmospheric data set applied in simulation S4 of EX-2. Conceptually, some information regarding the actual soil packing should inherently be retained as an artifact in the atmospheric data based on the differences in local evaporation rate between the sand layers. As would be expected from the results presented in sections 3.2 and 3.3 however, any associated local variability in the atmospheric conditions (see Figure 4) was not great enough to induce any longitudinal variability in the soil moisture and soil temperature distributions (not shown for brevity), illustrating instead the need for careful soil characterization. The simulations providing a description of the soil heterogeneity closest to the setup employed in Trautz et al. (2018) unsurprisingly provide the best estimate of the soil moisture/temperature distributions and cumulative water loss. As shown in Figure 8a, the error of the simulated cumulative water loss (shape and magnitude) grew quickly as the heterogeneity became more poorly described. Reducing the total volume of the coarse-textured soil by half (i.e., black line) was enough to cause the water loss to be underestimated by 1.5 kg. Assuming a homogeneous packing configuration consisting of the coarse-textured soil in lieu of the heterogeneous packing led to the overestimation of water losses by more than 7.5 kg.

Figure 8b provides a comparison of simulated water losses when the five surface undulations of EX-3 are no longer explicitly modeled (i.e., S4) but instead incorporated into a traditional atmospheric resistance term that replaces r_{bl} in the vapor flux boundary condition parameterization (equation 9) and is used in a new form of the sensible heat flux (equation 12) expressed here as

$$J_H = H = -\frac{\left(\rho C_p\right)_g}{r_a}\left[T - T_a(t)\right], \quad (19)$$

Aerodynamic resistance, r_a (s/m), is here defined according to (Thom, 1975)

$$r_a = \frac{1}{k^2 u_z}\left[\ln\left(\frac{z-d}{z_0}\right) - \psi(\zeta)\right]^2, \quad (20)$$

where k (=0.41) is the von Karman constant, u_z (m/s) is the wind speed measured at a height z (m), d (m) is the zero-plane displacement height taken to be 2/3 the height of the surface undulations (Brutsaert, 1982), z_0 (m) is the roughness length (Holmes, 2015), and ψ(ς) is a stability function; neutral atmospheric conditions were assumed so ψ(ς) was set equal to zero. Experimental wind speed, air temperature, and relative humidity data measured at a height of 0.4 m were provided as model inputs to the different spatial-discretization length intervals. Results are presented here for a simulation in which only a single point measurement was applied over the

full; there was little longitudinal variability in the atmospheric conditions at this height. These results show the importance of taking both the scale of the problem (i.e., micrometeorological heat and mass transfer) and the measurement location into consideration; any variability in the near-surface microclimate quickly disappears as one moves outside of the near-surface boundary layer that forms above the soil and the air becomes well-mixed. These results furthermore demonstrate that the conclusions reached in this study have not been biased by the adopted boundary condition parameterization but is also applicable to other approaches.

While it was not the intention, nor was there any theoretical foundation provided to directly extrapolate this work to the field scale, it is the hope of authors that the findings presented herein will have practical value in helping to inform experimental data collection strategies and modeling efforts across a wide scales ranging from the laboratory-column scale to the plot scale in the field setting for problems pertaining to bare-soil evaporation dynamics.

Acknowledgments

The design of the wind tunnel was made possible through the contributions of Jose Terrés-Nicoli at Orita and Boreas Wind Engineering and Philip Greenburg, the wind tunnel-porous media facility architect. The wind tunnel-porous media test facility and measurement protocol development was made possible with the assistance of Paul Schulte and the financial support from the Defense University Research Instrumentation Program (DURIP contract W911NF-06-1-0223), the National Science Foundation (EAR-10290690), the National Security Science and Engineering Fellowship (NSSEFF award FA9559-10-1-0139), and the AMAX Endowment. A.C.T. was supported by the U.S. Army Corps of Engineers Engineer Research and Development Center (ERDC) administered through an Oak Ridge Institute for Science and Education (ORISE) postdoctoral fellowship. Raw data for the experiments of Trautz et al. (2018) are publicly available and stored in the HydroShare digital repository https://doi.org/10.4211hs.b3177d0c45e547b18b486b45d17b75af.

References

Albertson, J. D., & Parlange, M. B. (1999). Surface length scales and shear stress: Implications for land-atmosphere interaction over complex terrain. *Water Resources Research*, 35(7), 2121– 2132. https://doi.org/10.1029/1999WR900094

Bear, J. (1972). *Dynamics of Fluids in Porous Media*. Mineola, USA: Dover.

Bénet, J., & Jouanna, P. (1982). Phenomenological relation of phase change of water in a porous medium: experimental verification and measurement of the phenomenological coefficient. *International Journal of Heat and Mass Transfer*, 25, 1747– 1754. https://doi.org/10.1016/0017-9310(82)90154-5

Berg, A., Findell, K., Lintner, B., Giannini, A., Seneviratne, S. I., van den Hurk, B., Lorenz, R., Pitman, A., Hagemann, S., Meier, A., Cheruy, F., Ducharne, A., Malyshev, S., & Milly, P. C. D. (2016). Land–atmosphere feedbacks amplify aridity increase over land under global warming. *Nature Climate Change*, 6(9), 869– 874. https://doi.org/10.1038/nclimate3029

Berge, H. F. M. (1990). *Heat Transfer in Bare Topsoil and the Lower Atmosphere*. Wageningen, Netherlands: PUDOC.

Betts, A. K. (2004). Understanding hydrometerology using global models. *Bulletin of the American Meteorological Society*, 85(11), 1673– 1688. https://doi.org/10.1175/BAMS-85-11-1673

Betts, A. K., Desjardins, R., Beljaars, A. C. M., & Tawfik, A. (2015). Observational study of land-surface-cloud-atmosphere coupling on daily timescales. *Frontiers of Earth Science*, 3(13), 1– 18. https://doi.org/doi:10.3389/feart.2015.00013

Bittelli, M., Ventura, F., Campbell, G. S., Snyder, R. L., Gallegati, F., & Pisa, P. R. (2008). Coupling of heat, water vapor, and liquid water fluxes to compute evaporation in bare soils. *Journal of Hydrology*, 362, 191– 205. https://doi.org/10.1016/j.jhydrol.2008.08.014

Brocca, L., Moramarco, T., Melone, F., Wagner, W., Hasenauer, S., & Hahn, S. (2012). Assimilation of surface- and root-zone ASCAT soil moisture products into rainfall-runoff models. *IEEE Transactions on Geoscience and Remote Sensing*, 50(7), 2,542– 2,555. https://doi.org/10.1109/TGRS.2011.2177468

Brutsaert, W. (1982). Evaporation into the atmosphere: Theory, history, and applications. Dordrecht, Netherlands: D. Reidel Company. https://doi.org/10.1007/978-94-017-1497-6

Campbell, G. S. (1985). *Soil Physics with BASIC*. New York: Elsevier.

Campbell, G. S., Jungbauer, J. D., Bidlake, W. R., & Hungerford, R. D. (1994). Predicting the effect of temperature on soil thermal-conductivity. *Soil Science*, 158(5), 307– 313. https://doi.org/10.1097/00010694-199411000-00001

Castellví, F. (2012). Fetch requirements using surface renewal analysis for estimating scalar surface fluxes from measurements in the inertial sublayer. *Agricultural and Forest Meteorology*, 152(15), 233– 239. https://doi.org/10.1016/j.agrformet.2011.10.004

Cebeci, T., & Smith, A. M. O. (1974). *Analysis of Turbulent Boundary Layers*. New York: Academic Press.

Chammari, A., Naon, B., Cherblanc, F., & Bénet, J. (2003). Transfert d'eau en sol aride avec changement de phase—Water transport with phase change at low water content. *Comptes Rendus Mécanique*, 331, 759– 765. https://doi.org/10.1016/j.crme.2003.07.005

Chen, F., & Zhang, Y. (2009). On the coupling strength between the land surface and the atmosphere: From viewpoint of surface exchange coefficients. *Geophysical Research Letters*, 36, L10404. https://doi.org/10.1029/2009GL037980

Davarzani, H., Smits, K., Tolene, R. M., & Illangasekare, T. (2014). Study of the effect of wind speed on evaporation from soil through integrated modeling of the atmospheric boundary layer and shallow subsurface. *Water Resources Research*, 50, 1– 20. https://doi.org/10.1002/2013WR013952

Davis, R. S. (1992). Equation for the determination of the density of moist air (1981/91). *Metrologia*, 29(1), 67– 70. https://doi.org/10.1088/0026-1394/29/1/008

Diremeyer, P. A., Koster, R. D., & Guo, Z. (2006). Do global models properly represent the feedback between land and atmosphere? *Journal of Hydrometeorology*, 7(1), 177– 1198. https://doi.org/10.1175/JHM532.1

Entekhabi, D., Reichle, R. H., Koster, R. D., & Crow, W. T. (2010). Performance metrics for soil moisture retrievals and application requirements. *Journal of Hydrometeorology*, 11(3), 832– 840. https://doi.org/10.1175/2010JHM1223.1

Fayer, M. J., & Simmons, C. S. (1995). Modified soil water retention functions for all matric suctions. *Water Resources Research*, 31, 1233– 1238. https://doi.org/10.1029/95WR00173

Ferguson, C. R., Wood, E. F., & Vinukollu, R. K. (2012). A global intercomparison of modeled and observed land-atmosphere coupling. *Journal of Hydrometeorology*, 13(3), 749– 784. https://doi.org/10.1175/JHM-D-11-0119.1

Fetzer, T., Smits, K. M., & Helmig, R. (2016). Effect of turbulence and roughness on coupled porous-medium/free-flow exchange processes. *Water Resources Research*, 114, 395– 424. https://doi.org/10.1007/s11242-016-0654-6

Gaikovich, K. P. (2000). Study of atmospheric-turbulence effects on the formation of a thermal film in the near-surface water layer and the dynamics of air-water heat exchange using measurements of thermal radio emission. *Radiophysics and Quantum Electronics*, 43(6), 469– 477. https://doi.org/10.1007/BF02677174

Haghighi, E., & Or, D. (2013). Evaporation from porous surfaces into turbulent airflows: Coupling eddy characteristics with pore scale vapor diffusion. *Water Resources Research*, 49, 8432– 8442. https://doi.org/10.1002/2012WR013324

Haghighi, E., & Or, D. (2015a). Evaporation from wavy porous surfaces into turbulent airflows. *Transport in Porous Media*, 110(2), 225– 250. https://doi.org/10.1007/s11242-015-0512-y

Haghighi, E., & Or, D. (2015b). Thermal signatures of turbulent airflows interacting with evaporating thin porous surfaces. *International Journal of Heat and Mass Transfer*, 87, 429– 446. https://doi.org/10.1016/j.ijheatmasstransfer.2015.04.026

Hamamoto, S., Moldrup, P., Kawamoto, K., Sakaki, T., Nishimura, T., & Komatsu, T. (2016). Pore network structure linked by X-ray CT to particle characteristics and transport parameters. *Soils and Foundations*, 56(4), 676– 690. https://doi.org/10.1016/j.sandf.2016.07.008

Hanks, R. J., Gardner, H. R., & Fairbourn, M. L. (1967). Evaporation of water from soils as influenced by drying with wind and radiation. *Soil Science Society of America Journal*, 31, 593– 598. https://doi.org/10.2136/sssaj1967.03615995003100050001x

Hide, J. C. (1954). Observations on factors influencing the evaporation of soil moisture. *Soil Science Society of America Proceedings*, 18(3), 234– 239. https://doi.org/10.2136/sssaj1954.03615995001800030002x

Hirschi, M., Mueller, B., Dorigo, W., & Seneviratne, S. I. (2014). Using remotely sensed soil moisture for land–atmosphere coupling diagnostics: The role of surface vs. root-zone soil moisture variability. *Remote Sensing of Environment*, 154, 246– 252. https://doi.org/10.1016/j.rse.2014.08.030

Ho, J. (2006). Vapor transport processes. In C. Ho & S. Webb (Eds.), *Gas Transport in Porous Media* (pp. 27– 46). Dordrecht, Netherlands: Springer.

Hohenegger, C., Brockhaus, P., Bretherton, C. S., & Schär, C. (2009). The soil moisture–precipitation feedback in simulations with explicit and parameterized convection. *Journal of Climate*, 22, 5003– 5020. https://doi.org/10.1175/2009JCLI2604

Holmes, J. D. (2015). *Wind Loading of Structures* (3rd ed.). Boca Raton, FL: CRC Press.

Holmes, J. W., Greacen, E. L., & Gurr, G. C. (1960). The evaporation of water from bare soils with different tilths. In *Transactions on 7th International Congress of Soil Science* (Vol. 1, pp. 188– 194). Wageningen, Netherlands: Society of Soil Science.

Horst, T. W., & Weil, J. C. (1994). How far is far enough? The fetch requirements for micrometeorological measurement of surface fluxes. *Journal of Atmospheric and Oceanic Technology*, 11, 10181025(4), 1018– 1025. https://doi.org/10.1175/1520-0426(1994)011<1018:HFIFET>2.0.CO;2

Illangasekare, T. H., Ramsey, J. L. Jr., Jensen, K. H., & Butts, M. B. (1995). Experimental study of movement and distribution of dense organic contaminants in heterogeneous aquifers. *Journal of Contaminant Hydrology*, 20(1–2), 1– 25. https://doi.org/10.1016/0169-7722(95)00045-W

Jackson, P. S., & Hunt, J. C. R. (1975). Turbulent wind flow over a low hill. *Quarterly Journal of the Royal Meteorological Society*, 101, 929– 955. https://doi.org/10.1002/qj.49710143015

Kato, H., Rodell, M., Beyrich, F., Cleugh, H., van Gorsel, E., Liue, H. Z., & Meyers, T. P. (2007). Sensitivity of land surface simulations to model physics, land characteristics, and forcings at four CEOP sites. *Journal of Meteorological Society of Japan*, 85A, 187– 204. https://doi.org/10.2151/jmsj.85A.187

Kell, G. S. (1975). Density, thermal expansivity, and compressibility of liquid water from 0° to 150°, Correlations and tables for atmospheric pressure and saturation reviewed and expressed on 1968 temperature scale. *Journal of Chemical and Engineering Data*, 20(1), 97– 105. https://doi.org/10.1021/je60064a005

Knist, S., Goergen, K., Buonomo, E., Christensen, O. B., Colette, A., Cardoso, R. M., Fealy, R., Fernández, J., García-Díez, M., Jacob, D., Kartsios, S., Katragkou, E., Keuler, K., Mayer, S., van Meijgaard, E., Nikulin, G., Soares, P. M. M., Sobolowski, S., Szepszo, G., Teichmann, C., Vautard, R., Warrach-Sagi, K., Wulfmeyer, V., & Simmer, C. (2016). Land-atmosphere coupling in EURO-CORDEX evaluation experiments. *Journal of Geophysical Research: Atmospheres*, 122, 79– 103. https://doi.org/10.1002/2016JD025476

Komori, S., Murakami, Y., & Ueda, H. (1989). The relationship between surface-renewal and bursting motions in an open-channel flow. *Journal of Fluid Mechanics*, 203, 103– 123. https://doi.org/10.1017/S0022112089001394

Koster, R. D., Guo, Z., Yang, R., Dirmeyer, P. A., Mitchell, K., & Puma, M. J. (2009). On the nature of soil moisture in land surface models. *Journal of Climate*, 22(16), 4322– 4335. https://doi.org/10.1175/2009JCLI2832.1

Lehmann, P., Assouline, S., & Or, D. (2008). Characteristic lengths affecting evaporative drying of porous media. *Physical Review E*, 77, 056309(5). https://doi.org/10.1103/PhysRevE.77.056309

Lehmann, P., & Or, D. (2009). Evaporation and capillary coupling across vertical contrasts in porous media. *Physical Review E*, 80, 046318(4). https://doi.org/10.1103/PhysRevE.80.046318

Lozano, A., Cherblanc, F., Cousinand, B., & Bénet, J. (2008). Experimental study and modeling of the water phase change kinetics in soils. *European Journal of Soil Science*, 59, 939– 949. https://doi.org/10.1111/j.1365-2389.2008.01050.x

Marek, R., & Straub, J. (2001). Analysis of the evaporation coefficient and the condensation coefficient of water. *International Journal of Heat and Mass Transfer*, 44(1), 39– 53. https://doi.org/10.1016/S0017-9310(00)00086-7

McInnes, K. J., Heilman, J. L., & Savage, M. J. (1994). Aerodynamic conductances along a bare ridge-furrow tilled soil surface. *Agricultural and*

Forest Meteorology, 68, 119– 131. https://doi.org/10.1016/0168-1923(94)90031-0

Meek, R. L., & Baer, A. D. (1970). The periodic viscous sublayer model and heat transfer to drag reducing solutions. *AlChE Journal*, 16(6), 1100– 1102. https://doi.org/10.1002/aic.690160642

Millington, R. J., & Quirk, J. M. (1961). Permeability of porous solids. *Transactions of the Faraday Society*, 57, 1200– 1207. https://doi.org/10.1039/tf9615701200

Monteith, J. L. (1981). Evaporation and surface temperature. *Quarterly Journal of the Royal Meteorological Society*, 107(451), 1– 27. https://doi.org/10.1002/qj.49710745102

Mosthaf, K., Baber, K., Flemisch, B., Helmig, R., Leijnse, A., Rybak, I., & Wohlmuth, B. (2011). A coupling concept for two-phase compositional porous-medium and single-phase compositional free flow. *Water Resources Research*, 47, W10522. https://doi.org/10.1029/2011WR010685

Mualem, Y. (1976). A new model for predicting the hydraulic conductivity of unsaturated porous media. *Water Resources Research*, 12(3), 513– 522. https://doi.org/10.1029/WR012i003p00513

Or, D., Lehmann, P., Shahraeeni, E., & Shokri, N. (2013). Advances in soil evaporation physics—A review. *Vadose Zone Journal*, 12(4). https://doi.org/10.2136/vzj2012.0163

Ouedraogo, F., Cherblanc, F., Naon, B., & Bénet, J. C. (2013). Water transfer in soil at low water content. Is the local equilibrium assumption still appropriate? *Journal of Hydrology*, 492, 117– 127. https://doi.org/10.1016/j.jhydrol.2013.04.004

Philip, J. R., & de Vries, V. D. (1957). Moisture movement in porous materials under temperature gradient. *Eos Transactions AGU*, 38(2), 222– 232. https://doi.org/10.1029/TR038i002p00222

Picotte, J. J., Rosenthal, D. M., Rhode, J. M., & Cruzan, M. B. (2007). Plastic responses to temporal variation in moisture availability: Consequences for water use efficiency and plant performance. *Oecologia*, 153(4), 821– 832. https://doi.org/10.1007/s00442-007-0794-z

Poling, B. E., Prausnitz, J. M., & O'Connell, J. P. (2001). *The Properties of Liquids and Gases* (5th ed.). New York: McGraw Hill.

Pope, S. B. (2000). *Turbulent Flows*. Cambridge, UK: Cambridge University Press.

Prunty, L., & Horton, R. (1994). Steady-state temperature distribution in nonisothermal unsaturated closed soil cells. *Soil Science Society of America Journal*, 58, 1358– 1363. https://doi.org/10.2136/sssaj1994.03615995005800050011x

Rodriguez-Iturbe, I., Porporato, A., Laio, F., & Ridolfi, I. (2001). Plants in water-controlled ecosystems: Active role in hydrologic processes and response to water stress I. Scope and general outline. *Advances in Water Resources*, 24(7), 695– 705. https://doi.org/10.1016/S0309-1708(01)00004-5

Ruiz, T., & Bénet, J. C. (2001). Phase change in a heterogeneous medium: Comparison between the vaporization of water and heptanes in an unsaturated soil at two temperatures. *Transport in Porous Media*, 44, 337– 353. https://doi.org/10.1023/A:101077392

Sakaki, T., & Illangasekare, T. H. (2007). Comparison of height-averaged and point-measured capillary pressure-saturation relations for sands using a modified Tempe cell. *Water Resources Research*, 43, W12502. https://doi.org/10.1029/2006WR005814

Sakaki, T., Plampin, M. R., Pawar, R., Komatsu, M., & Illangasekare, T. H. (2013). What controls carbon dioxide gas phase evolution in the subsurface? Experimental observations in a 4.5 m-long column under different heterogeneity conditions. *International Journal of Greenhouse Gas Control*, 17, 66– 77. https://doi.org/10.1016/j.ijggc.2013.03.025

Santanello, J. A. Jr., Peters-Lidard, C. D., Kumar, S. V., Alonge, C., & Tao, W. K. (2009). A modeling and observational framework for diagnosing local land-atmosphere coupling on diurnal time scales. *Journal of Hydrometeorology*, 10(3), 577– 599. https://doi.org/10.1175/2009JHM1066.1

Schlichting, H., & Gersten, K. (2017). *Boundary Layer Theory* (9th ed.). Heidelberg, Germany: Springer-Verlag.

Schlünder, E. U. (1988). On the mechanism of the constant drying rate period and its relevance to diffusion controlled catalytic gas phase reactions. *Chemical Engineering Science*, 43(10), 2685– 2688. https://doi.org/10.1016/0009-2509(88)80012-5

Schroth, M. H., Istok, J. D., Ahearn, S. J., & Selker, J. S. (1996). Characterization of Miller-similar silica sands for laboratory hydrologic studies. *Soil Science Society of America Journal*, 60(5), 1331– 1339. https://doi.org/10.2136/sssaj1996.03615995006000050007x

Shahraeeni, E., Lehmann, P., & Or, D. (2012). Coupling of evaporative fluxes from drying porous surfaces with air boundary layer: Characteristics of evaporation from discrete pores. *Water Resources Research*, 48, W09525. https://doi.org/10.1029/2012WR011857

Shiklomanov, I. A. (1993). World fresh water resource. In P. H. Gleick (Ed.), *Water Crisis: A Guide to World Fresh Water Resources* (pp. 13– 24). Cambridge, UK: Oxford University Press.

Shokri, N., Lehmann, P., Vontobel, P., & Or, D. (2008). Drying front and water content dynamics during evaporation from sand delineated by neutron radiography. *Water Resources Research*, 44, W06418. https://doi.org/10.1029/2007WR006385

Shokri, N., & Or, D. (2011). What determines drying rates at the onset of diffusion controlled stage-2 evaporation from porous media? *Water Resources Research*, 47, W09513. https://doi.org/10.1029/2010WR010284

Speight, J. G. (2005). *Lange's Handbook of Chemistry* (6th ed.). New York: McGraw-Hill.

Taylor, C. M., & Ellis, R. J. (2006). Satellite detection of soil moisture impacts on convection at the mesoscale. *Geophysical Research Letters*, 33, L03404. https://doi.org/10.1029/2005GL025252

Thom, A. S. (1972). Momentum, mass, and heat exchange of vegetation. *Quarterly Journal of the Royal Meteorological Society*, 98(415), 124– 124, 134. https://doi.org/10.1002/qj.49709841510

Thom, A. S. (1975). Momentum, mass and heat exchange of plant communities. In J. L. Monteith (Ed.), *Vegetation and the Atmosphere* (Vol. 1, pp. 57– 109). London, UK: Academic Press.

Trautz, A. C. (2015). *Heat and mass transfer in porous media under the influence of near-surface boundary layer atmospheric flow (Doctoral Thesis)*. Golden CO: Colorado School of Mines.

Trautz, A. C., Illangasekare, T. H., & Howington, S. (2018). Experimental testing scale considerations for the investigation of bare-soil evaporation dynamics in the presence of sustained above-ground airflow. *Water Resources Research*, 54, 8963– 8982. https://doi.org/10.1029/2018WR023102

Trautz, A. C., Illangasekare, T. H., & Rodriguez-Iturbe, I. (2017). Role of co-occurring competition and facilitation in plant spacing hydrodynamics in water-limited environments. *Proceedings of the National Academy of Sciences*, 114(35), 9379– 9384. https://doi.org/10.1073/pnas.1706046114

Trautz, A. C., Illangasekare, T. H., Rodriguez-Iturbe, I., Heck, K., & Helmig, R. (2017). Development of an experimental approach to study coupled soil-plant-atmosphere processes using plant analogs. *Water Resources Research*, 53, 3319– 3340. https://doi.org/10.1002/2016WR019884

Trautz, A. C., Smits, K. S., & Cihan, A. (2015). Continuum-scale investigation of evaporation from bare soil under different boundary and initial conditions: An evaluation of nonequilibrium phase change. *Water Resources Research*, 51, 7630– 7648. https://doi.org/10.1002/2014WR016504

Trigo, I. F., Boussetta, S., Viterbo, P., Balsamo, G., Beljaars, A., & Sandu, I. (2015). Comparison of model land skin temperature with remotely sensed estimates and assessment of surface atmosphere coupling. *Journal of Geophysical Research: Atmosphere*, 120, 12,096– 12,111. https://doi.org/10.1002/2015JD023812

van Brakel, J. (1980). Mass transfer in convective drying. In *Advances in Drying* (Vol. 1, pp. 217– 267). Washington, DC: Hemisphere Publishing Corporation.

van de Griend, A. A., & Owe, M. (1994). Bare soil surface resistance to evaporation by vapor diffusion under semiarid conditions. *Water Resources Research*, 30(2), 181– 188. https://doi.org/10.1029/93WR02747

van Genuchten, M. T. (1980). A closed-form equation for predicting the hydraulic conductivity of unsaturated soils. *Soil Science Society of America Journal*, 44(5), 892– 898. https://doi.org/10.2136/sssaj1980.03615995004400050002x

Veihmeyer, F. J. (1938). Evaporation from soils and transpiration. *Eos, Transactions of the American Geophysical Union*, 19(2), 612– 619. https://doi.org/10.1029/TR019i002p00612

Villagarcía, L., Were, A., Domingo, F., García, M., & Alados-Arboledas, L. (2007). Estimation of soil boundary-layer resistance in sparse semiarid stands for evapotranspiration modelling. *Journal of Hydrology*, 342(1–2), 173– 183. https://doi.org/10.1016/j.jhydrol.2007.05.023

Wagner, C., Kenjeres, S., & von Rohr, P. R. (2011). Dynamic large eddy simulations of momentum and wall heat transfer in forced convection over wavy surfaces. *Journal of Turbulence*, 12, N7. https://doi.org/10.1080/14685248.2010.547496

Western, A. W., Zhou, S.-L., Grayson, R. B., McMahoun, T. A., Blöschl, G., & Wilson, D. J. (2004). Spatial correlation of soil moisture in small catchments and its relationship to dominant spatial hydrological processes. *Journal of Hydrology*, 286(1–4), 113– 134. https://doi.org/10.1016/j.jhydrol.2003.09.014

Whitaker, S. (1977). Simultaneous heat, mass, and momentum transfer in porous media. A theory of drying. *Advances in Heat Transfer*, 13, 119– 203. https://doi.org/10.1016/S0065-2717(08)70223-5

Willis, W. O., & Bond, J. J. (1971). Soil water evaporation: Reduction by simulated tillage. *Soil Science Society of America Proceedings*, 35, 526– 528. https://doi.org/10.2136/sssaj1971.03615995003500040016x

Yiotis, A. G., Boudouvis, A. G., Stubos, A. K., Tsimpanogiannis, I. N., & Yortsos, Y. C. (2004). Effect of liquid films on the drying of porous media. *AICHE Journal*, 50(11), 2721– 2737. https://doi.org/10.1002/aic.10265

Yiotis, A. G., Stubos, A. K., Boudouvis, A. G., & Yortsos, Y. C. (2001). A 2-D pore-network model of the drying of single-component liquids in porous media. *Advances in Water Resources*, 24, 439– 460. https://doi.org/10.1016/S0309-1708(00)00066-X

Yiotis, A. G., Tsimpanogiannis, I. N., Stubos, A. K., & Yortsos, Y. C. (2006). Pore-network study of the characteristic periods in the drying of porous

materials. *Journal of Colloid Interface Science*, 297(2), 738– 748. https://doi.org/10.1016/j.jcis.2005.11.043

Yiotis, A. G., Tsimpanogiannis, I. N., Stubos, A. K., & Yortsos, Y. C. (2007). Coupling between external and internal mass transfer during drying of a porous medium. *Water Resources Research*, 43, W06403. https://doi.org/10.1029/2006WR005558

Zeng, Y., Su, Z., Wan, L., & Wen, J. (2011). Numerical analysis of air-water-heat flow in unsaturated soil: Is it necessary to consider airflow in land surface models. *Journal of Geophysical Research*, 116, D20107. https://doi.org/10.1029/2011JD015835

Zhang, J., & Datta, A. K. (2004). Some considerations in modeling of moisture transport in heating of hygroscopic materials. *Drying Technology*, 22, 1983–2008. https://doi.org/10.1081/DRT-200032740